Electrochimica Acta 444 (2023) 142032

Contents lists available at ScienceDirect

Electrochimica Acta

journal homepage: www.journals.elsevier.com/electrochimica-acta

Isopropanol electro-oxidation on Pt-Ru-Ir: A journey from model thin-film libraries towards real electrocatalysts

Mária Minichová [a,b,*], Chuyen Van Pham [a], Bin Xiao [d], Alan Savan [d], Andreas Hutzler [a], Andreas Körner [a], Ivan Khalakhan [e], Miquel Gamón Rodríguez [e], Iosif Mangoufis-Giasin [a,b], Valentín Briega-Martos [a], Attila Kormányos [a,c], Ioannis Katsounaros [a], Karl J.J. Mayrhofer [a,b], Alfred Ludwig [d], Simon Thiele [a,b], Serhiy Cherevko [a,*]

[a] Forschungszentrum Jülich GmbH, Helmholtz Institute Erlangen-Nürnberg for Renewable Energy (IEK-11), Cauerstr. 1, Erlangen 91058, Germany
[b] Department of Chemical and Biological Engineering, Friedrich-Alexander-Universität Erlangen-Nürnberg, Egerlanstr. 3, Erlangen 91058, Germany
[c] Department of Physical Chemistry and Materials Science, Interdisciplinary Excellence Centre, University of Szeged, Szeged H-6720, Hungary
[d] Chair for Materials Discovery and Interfaces, Institute for Materials, Ruhr University Bochum, Bochum, Germany
[e] Department of Surface and Plasma Science, Faculty of Mathematics and Physics, Charles University, V Holešovičkách 2, 18000 Prague 8, Czech Republic

ARTICLE INFO

Keywords:
Fuel cell
Electrocatalysis
Alcohol oxidation
Stability
ICP-MS

ABSTRACT

Liquid fuels are considered a promising alternative to hydrogen in proton exchange membrane fuel cells. In particular, isopropanol, which can be selectively oxidised to acetone and further hydrogenated back to isopropanol using electrochemical and heterogeneous catalysis routes, respectively, opens the possibility of zero-emission fuel cell operation without complex management of molecular H_2. However, the maximum electric power of such fuel cells is still relatively low, which is attributed to the poisoning of state-of-the-art Pt-Ru electrocatalysts by adsorbed acetone and/or Ru oxide/hydroxide. Here, in order to mitigate Pt-Ru poisoning at higher anodic potentials during isopropanol oxidation in acidic media, the effect of the addition of Ir, a less oxophilic element than Ru, on the activity and stability during dynamic experiments of Pt-Ru is systematically investigated. To identify the most active compositions, Pt-Ru-Ir thin-film material libraries are prepared using magnetron co-sputtering. The electrocatalytic activity of the libraries is screened using a high-throughput scanning flow cell setup. Catalysts with the highest activity are further synthesised in the form of carbon-supported nanoparticles. Comparing the two systems, similar trends are observed, highlighting the model material libraries being an excellent starting point for novel catalyst development. Besides electrocatalytic activity, catalyst shelf-life and dissolution stability are studied. While significant ageing in the air is found, partial reactivation is possible using a reductive treatment. The dissolution of the most promising nanoparticulate electrocatalyst is evaluated using online inductively coupled plasma mass spectrometry to assess the effect of Ir addition on Pt and Ru stability. No significant stabilising role of Ir, however, is observed. Hence, further optimisation of Pt-Ru or Pt-Ru-Ir is still needed to improve isopropanol fuel cell performance.

1. Introduction

Transportation belongs to one of the largest energy-demanding sectors worldwide. Currently, it is also one of the largest greenhouse gas emitters [1]. Shifting towards sustainable mobility, meaning the energy comes only from renewable resources, would be crucial in reaching the 21st-century energy and climate goals. Together with batteries, green hydrogen serves as an alternative energy carrier in transportation, as evidenced by successful implementations of fuel cell technologies in cars. However, considering current dependencies on liquid fuels and an existent infrastructure for their transport and storage, green hydrogen would reach its limitations due to its gaseous nature [2]. Fuels benefiting from the existing infrastructure would be alcohols. Namely, isopropanol is particularly interesting due to a recently introduced option of coupling the direct isopropanol fuel cell (DIFC) to a hydrogenation unit with liquid organic hydrogen carriers (LOHC). This allows the

* Corresponding authors at: Forschungszentrum Jülich GmbH, Helmholtz Institute Erlangen-Nürnberg for Renewable Energy (IEK-11), Cauerstr. 1, Erlangen 91058, Germany.
E-mail addresses: m.minichova@fz-juelich.de (M. Minichová), s.cherevko@fz-juelich.de (S. Cherevko).

https://doi.org/10.1016/j.electacta.2023.142032
Received 11 November 2022; Received in revised form 2 February 2023; Accepted 9 February 2023
Available online 12 February 2023

subsequent hydrogenation of the oxidation product, acetone, resulting in a thermo-neutral process [3]. Compared to regular direct alcohol fuel cells, where the main oxidation product is CO_2, isopropanol oxidation is almost 100% selective towards acetone, which opens up an option for acetone recycling leading to a carbon-neutral process [3].

Commonly used anode catalysts for an alcohol electro-oxidation reaction in acidic media are materials based on Pt, such as Pt-Ru [4–6], Pt-Pd [7,8], or Pt-Sn [9–11]. It was observed that adding a second (or third) metal to Pt can lead to increased activity and decreased catalyst poisoning by tuning the adsorption energy of intermediates [12–18]. The state-of-the-art binary anode catalyst for proton exchange membrane (PEM) alcohol fuel cells up till now is Pt-Ru [19]. It was also predominantly tested for the case of isopropanol oxidation [3,20–22]. Comparing different alcohols in PEM fuel cells using Pt-Ru catalysts, isopropanol was oxidised at the lowest overpotential (0.15 V) [20], yielding a higher open circuit voltage (OCV) and power output of PEM fuel cells [23]. Contrary to advantageous low overpotentials attributed to Ru active sites, the attained currents also reached low maximum values due to poisoning of the active sites by acetone (or carbon-based intermediates) and/or oxidation of Ru, which both led to subsequent activity loss of the catalyst [20,22]. Here, the appearance of the additional peak in secondary alcohols was recently attributed to stabilisation by the presence of Ru of an O-bonded intermediate that lowers the onset potential of the reaction [21].

Alloying Pt-Ru with another metal could mitigate the poisoning effect and increase the activity of the catalyst (by facilitating CO oxidation or desorption) and is a common strategy in methanol oxidation. Therefore, many different third metal alloys with Pt-Ru, such as Au, Cu, Fe, Ag, Pd, W, Mo, Co, Ni, Sn, Os, Rh, Pb, Bi, and Ir, were already tested [24–35]. In particular, the addition of Ir, a less noble metal than Pt but also less oxophilic than Ru (potentially resulting in suppressed poisoning), seems like a viable option [36]. The literature reports on Pt-Ru-Ir in electrocatalysis are dominant for certain reactions, but the opposite is true for the oxidation of secondary alcohols. For instance, the incorporation of Ir in Pt-Ru nanoparticles resulted in increased activity for oxygen evolution and reduction reactions (OER and ORR) [37–39]. More importantly, it was also observed that adding Ir to Pt-Ru/C nanoparticles can lead to better dispersion of metallic compounds, where OH groups can likely be stabilised at the metallic Ir surface, thus assisting in the oxidation of adsorbed intermediates in methanol oxidation [30]. Similarly, it was reported that crystallinity could play a role in increasing activity towards methanol oxidation and mitigation of CO poisoning [40]. The dependence of methanol oxidation activity on the amount of Ir for $Pt_1Ru_1Ir_x$/C nanoparticles was also studied. The results revealed a higher activity and better catalyst durability with increasing Ir content by Ir suppressing the dissolution of Ru [36,41]. Clear evidence of enhanced activity of OER, ORR, and methanol oxidation suggests that ternary Pt-Ru-Ir could also be a better catalyst for the anode oxidation of isopropanol. Based on all mentioned above, we could expect further stabilisation of the O-bounded intermediate by lowering the onset potential increasing the reaction rate and promoting the desorption of acetone.

When considering the activity of a particular alloy towards any reaction, the ratio of metals has to be taken into account as not every combination is active (e.g. the bifunctional role between Pt and Ru can be enhanced but also lost by adding Ir). Magnetron sputtered thin-film material libraries, in combination with the scanning flow cell (SFC) [41,42], allow high-throughput activity screening with spatial resolution. For instance, in recent works with binary alloys, the study of ORR on a Pt-Cu thin-films library led to the conclusion that Cu content is only beneficial from 20 atomic percent (at%) to 57 at% [43]. Similarly, the activity of isopropanol oxidation using a Pt-Ir library showed the most active composition to be around 3.4 at% Ir, the latter being necessary to achieve a higher oxidation current compared to pure Pt. When Ir content reached 30 at%, a new peak appeared (similarly to Pt-Ru), although currents obtained at these lower overpotentials were negligible compared to Pt-Ru [44]. Together with the mentioned findings from alcohol oxidation, this is another reason to explore a combination of these three elements for isopropanol oxidation. As ternary alloys offer more options of possible compositions than binary alloys, the need for rapid activity screening of a multitude of compositions is indispensable.

In this work, we systematically study the composition dependence of Pt-Ru-Ir catalyst activity of isopropanol oxidation using magnetron-sputtered thin-films. We identified the most active composition and synthesised carbon-supported $Pt_1Ru_1Ir_x$ alloy nanostructures with various Ir content. We evaluated the transferability of the observed activity trends attained from the sputtered thin-film material library, serving as a model system, to carbon-supported nanoparticles (synthesised in-house) that can be used in applications. To evaluate whether the addition of Ir also plays a role in stabilising Pt and Ru in the most active catalyst composition, we conducted ICP-MS measurements coupled with SFC to identify the onset potential of dissolution of each element. This technique also allowed tracking activity in a high throughput manner, especially for thin-film samples [45].

2. Experimental section

2.1. Materials

Pt_1Ru_1/C commercial nanoparticles (details on the catalyst characteristics are summarised in our previous work [20]) were provided by Tanaka. $HClO_4$ (70%, Suprapur®), isopropanol (ACS, 99.5+%, VWR), and ionomer solution (5 wt.% Nafion, Sigma-Aldrich) were purchased from Merck and used without further purification. Ar (99.999%) and H_2 (99.999%) were purchased from Air Liquide Deutschland GmbH. Solutions were prepared using ultrapure water (18.2 MΩ, TOC < 3 ppb) provided by a Merck Millipore MilliQ system.

2.2. Combinatorial synthesis of Pt-Ru-Ir and Ru-Ir thin-film material libraries

Two thin-film libraries, Pt-Ru-Ir and Ru-Ir, were fabricated using combinatorial magnetron co-sputtering from elemental targets. The deposition was performed at room temperature using Ir (purity 99.99%), Pt (purity 99.99%), and Ru (purity 99.99%) metallic targets (4-inch diameter). As substrates, Si/SiO_2 wafers with 100 mm diameter were used. A 15 nm thick Ti adhesion layer was coated on the substrate prior to the deposition of the materials libraries. To obtain a continuous compositional gradient, the substrate was kept stationary, and each target was inclined with an angle of 45° with respect to the substrate. Prior to the deposition, the chamber vacuum was on the order of 10^{-8} Torr. The material libraries were deposited at a pressure of 20 mTorr with an Ar flow of 80 sccm. Table 1 lists the process parameters used to fabricate the material libraries.

The obtained material libraries comprise 342 regions of interest (ROIs). Each ROI has a size of 4.5 mm x 4.5 mm. All ROIs experience the same experimental treatment, which enables us to systematically investigate correlations between composition and properties, increasing throughput and substantially decreasing errors related to sample-to-sample variation.

2.2.1. High-throughput characterisation of the material libraries

Compositions and phase constitution for all 342 ROIs in the as-deposited Pt-Ru-Ir material library were investigated using automated, high-throughput characterisation techniques. The elemental

Table 1
Sputtering parameters for the materials libraries Pt-Ru-Ir and Ru-Ir, respectively.

Materials library	Ir [W]	Pt_{RF} [W]	Ru_{DC} [W]	Deposition time [s]
Pt-Ru-Ir	56 (DC)	169	66	800
Ru-Ir	245 (RF.)	–	140	800

compositions were determined using automated energy dispersive X-ray spectroscopy (EDXS) conducted on a JEOL 5800 scanning electron microscope (SEM). 20 kV accelerating voltage, a spot size of 50 μm, and a 10 mm working distance with acquisition times of 60 s for each ROI were used during the measurement. The excited X-ray energy lines for constituent elements are Ir Lα (9.174 keV), Pt Lα (9.441 keV), and Ru Kα (19.233 keV). The analysis of EDXS data was performed based on the standard ZAF-correction process provided by the INCA Energy software (Oxford Instruments). The software was calibrated for quantification using a Co standard. High-throughput phase analysis was done using X-ray diffraction (XRD) (Bruker D8 Discover, equipped with a VANTEC-500 area detector, Cu Kα radiation, with a sample-to-detector distance of 149 mm). The X-ray beam size is collimated to 1 mm (collimator diameter = 1 mm with a divergence of below 0.007°). An area detector was used to collect the diffraction data, and three frames were collected for each measured area. These frames were integrated into one-dimensional data sets by using DIFFRAC.EVA software was provided by Bruker and was then used for phase identification. The phases were identified by comparing the measured patterns with references from the Inorganic Crystal Structure Database (ICSD).

2.2.2. Laser profilometry

Surface roughness was measured by a laser scanning microscope (LSM), Keyence VK-X100K. This method was used to establish the roughness of the thin-film material library. The area of the measurement was chosen to be the same for each surface measurement throughout the library.

2.3. Synthesis and characterisation of nanoparticles

2.3.1. Synthesis

The synthesis of $Pt_1Ru_1Ir_x$ ($x = 0.25$, 0.5, 1.0, and 1.5) nanoparticles supported on carbon particles ($Pt_1Ru_1Ir_x$/C) was carried out as follows: The exact loading of each metal can be found in Table S1. First, 97.5 mg of Pt/C (40 wt% Pt, Hispec) was added to a spherical glass, and then 1 ml H_2O was added to wet the catalysts. Subsequently, 20 mL isopropanol was added, followed by a sonication step for 10 min to disperse the Pt/C precursor. The solution was stirred for 1 h at 75 °C. A salt precursor solution was prepared by dissolving the hydrated $RuCl_3$ and $IrCl_3$ in 1 mL water by sonication for 2 min. Next, 1 mL aqueous solution containing 50.5 mg hydrated $RuCl_3$ (38–42 wt% Ru, Sigma Aldrich) and a predetermined amount (according to Ir content, x) of $IrCl_3$ (53.66 wt% Ir) was added to the reaction solution under stirring. Deposition of Ru and Ir on Pt nanoparticles took place in the reaction solution by continuous stirring at 600 rpm for 3 h at 75 °C. The reaction solution was then filtered and rinsed with copious amounts of H_2O using a filtration system and freeze-dried for six h. An annealing step was applied in a reductive gas mixture of 10% H_2 in Ar at 350 °C for 2 h.

2.3.2. Transmission electron microscopy

Samples for transmission electron microscopy (TEM) were prepared by dip-coating TEM grids with suspensions of $Pt_1Ru_1Ir_x$/C powder in isopropanol and water, followed by drying in the air and remote air plasma cleaning for 1 min utilising a Tergeo EM plasma cleaner (PIE Scientific). Conventional and high-resolution TEM, high-angle annular dark field (HAADF) scanning TEM (STEM), and spectrum images using EDXS were acquired using a Talos F200i (Thermo Fisher Scientific, former FEI). The microscope, equipped with a Schottky emitter and two Bruker XFlash 6T-100 EDS detectors, was operated at an acceleration voltage of 200 kV. Data evaluation was performed using Velox.

2.3.3. XPS measurements

The XPS measurements were performed using an EnviroESCA system (SPECS Surface Nano Analysis, GmbH Germany) with a monochromated Al K_α X-ray source (1486.6 eV). The analyser Specs PHOIBOS hemispherical energy is kept under ultra-high vacuum conditions (10^{-9} mbar). The samples were stuck to the stainless-steel sample holder using carbon tape, and the spot size was about 200 μm. During XPS measurements, the core-level spectra of Pt 4f, Ir 4f, Ru 3d, Ru 3p, C 1s, O 1s, and F 1s were recorded with a pass energy of 20 eV, step size of 0.1 eV and dwell time of 0.3 s. The measured XPS spectra were processed using the KolXPD software (Kolibrik.net, Czech Republic).

2.3.4. SEM-EDXS measurements

The samples for SEM-EDXS composition analysis were prepared by drop-casting the nanoparticle catalyst dispersion onto silicon wafers, followed by drying on a hotplate. The catalyst dispersion was prepared by dispersing the catalyst powder in an isopropanol-water (1:1) mixture with ultrasonication for 2 min.

The compositional analysis of the catalyst powder was performed using a Crossbeam 540, Zeiss, SEM with an EDXS-detector (X-Max 150 silicon drift detector, Oxford Instruments). The energy dispersive spectra were obtained when applying a voltage of 20 kV.

2.4. Electrochemical measurements

2.4.1. Electrocatalytic activity measurements

All electrochemical measurements were performed in an acidic environment. A 0.1 M $HClO_4$ solution was used for blank measurements. For experiments with isopropanol, the acid concentration was maintained, and the concentration of isopropanol was kept at 0.1 M. Measurements were carried out in a custom-designed, home-built SFC [41]. The Pt-Ru-Ir thin-film material library or $Pt_1Ru_1Ir_x$/C nanoparticles were employed as the working electrode. Prior to electrochemical measurements, nanoparticulate catalysts were immobilised on a glassy carbon substrate as follows: The ink prepared by mixing 3 ml water/-isopropanol (4/1 v/v%), 2 μL of Nafion, and the corresponding amounts of nanoparticles to obtain 20–25 μg/cm^2 total metal loading was drop-casted (0.2 μL) onto polished glassy-carbon (GC). At the same time, a glassy-carbon rod (HTW, Sigradur G) was used as a counter electrode connected to the SFC on the electrolyte inlet side. An Ag/AgCl/3 M KCl electrode (Metrohm) was utilised as a reference electrode, which was connected to the SFC through a capillary channel on the outlet side, close to the working electrode surface. This configuration prevented the contamination of the electrolyte with Cl^- ions [46]. The potential of the reversible hydrogen electrode was controlled by purging with H_2 before activity measurements. The value obtained on the Pt disc electrode at OCV in the H_2 atmosphere was used to convert the potentials measured at Ag/AgCl reference electrode to the reversible hydrogen electrode (RHE) scale.

A Gamry Reference 600 potentiostat was used to carry out all electrochemical protocols. The working electrode was connected with an XYZ translation stage (Physik Instrumente M-403), which allowed the rapid screening of each electrocatalyst composition by displacing the SFC onto the different spots previously drop-casted on the GC plate. A stable electrolyte flow was maintained using a peristaltic pump (Ismatec). All instruments (stages, peristaltic pump, and gas control box) were controlled via custom-designed LabView software. A potentiodynamic experiment was started for activity screening at each of the different regions of interest. The protocol consisted of 3 fast cyclic voltammetry curves (CVs) starting at 0.05 V_{RHE} towards 1.5 V_{RHE} as the upper potential limit (UPL) with a scan rate of 200 mV s^{-1} to clean the surface. Subsequently, a slower CV from 0.05 V_{RHE} to 1.4 V_{RHE} for thin-films and 1 V_{RHE} for nanoparticles was acquired, with a scan rate of 50 mV s^{-1}. These protocols were used to map the activity of Pt-Ru-Ir with various compositions toward the oxidation of isopropanol

2.4.2. CO-stripping measurements

The CO-stripping experiments were conducted in an RDE setup using a custom-made Teflon cell and a PINE MSR Electrode Rotator. PtRuIr/C nanoparticles were employed as the working electrode. Prior to electrochemical measurements, nanoparticulate catalysts were immobilised

on a glassy-carbon RDE tip as follows: The tip was first polished using diamond paste and a polishing pad applying circular movement for 5 min, then washed with ultrapure water. The ink was prepared by mixing 3 ml water/isopropanol (4/1 v/v%), 2 μL of Nafion, and the corresponding amounts of nanoparticles to obtain 25 μg/cm^2 total metal loading was drop-casted (10 μL) onto the polished glassy-carbon tip. A glassy carbon rod was used as a counter electrode, and an Ag/AgCl/3 M KCl electrode (Metrohm) was utilised as a reference electrode. The value obtained on the Pt electrode at OCV in the H_2 atmosphere was used to convert the potentials measured at Ag/AgCl reference electrode to the reversible hydrogen electrode (RHE) scale. Measurements were conducted in an acidic environment (0.1 M $HClO_4$). A Gamry (Reference 600) potentiostat was used to carry out all electrochemical protocols. Before the CO-stripping experiment, the electrolyte was purged by Ar, and three cyclic voltammetry curves (CVs) starting at 0.05 V_{RHE} and going to 0.9 V_{RHE} with a scan rate of 20 mV s^{-1} were recorded. Subsequently, CO gas was purged into the electrolyte for 15 min to ensure the full surface coverage of the catalyst. Ar in high flow rate was used to clean reminding CO from the gas line and then purged into electrolyte for 35 min to remove remaining, not adsorbed CO. Finally, identical CVs (as before the experiment) were recorded in Ar atmosphere to evaluate ECSA from the CO-stripping experiment.

2.5. Online SFC/ICP-MS measurements

The dissolution of nanoparticulate electrocatalysts was studied by coupling the electrolyte outlet of the SFC to an ICP-MS (PerkinElmer, NexION 350x). The purged electrolyte flow rate was controlled (quantified at the beginning of each measurement day) by the peristaltic pump of the ICP-MS (MP2 pump, Elemental Scientific). The average flow rate was 3.76 ± 0.05 μl s^{-1}. The ICP-MS was calibrated daily by a four-point calibration slope made from standard solutions (Pt, Ru, Ir), which contained the metal ions of interest in each concentration range (0 – 5 μg L^{-1}) and 0.1 M $HClO_4$. ^{187}Re and ^{103}Rh (10 μg L^{-1}) served as the internal standards. The solution from the SFC and the solution containing internal standards were mixed in a Y-connector, introduced in the spray chamber, and subsequently in the ICP-MS. The measurements were performed in an acidic environment (0.1 M $HClO_4$) with and without isopropanol (0.05 M due to instrument limitations).

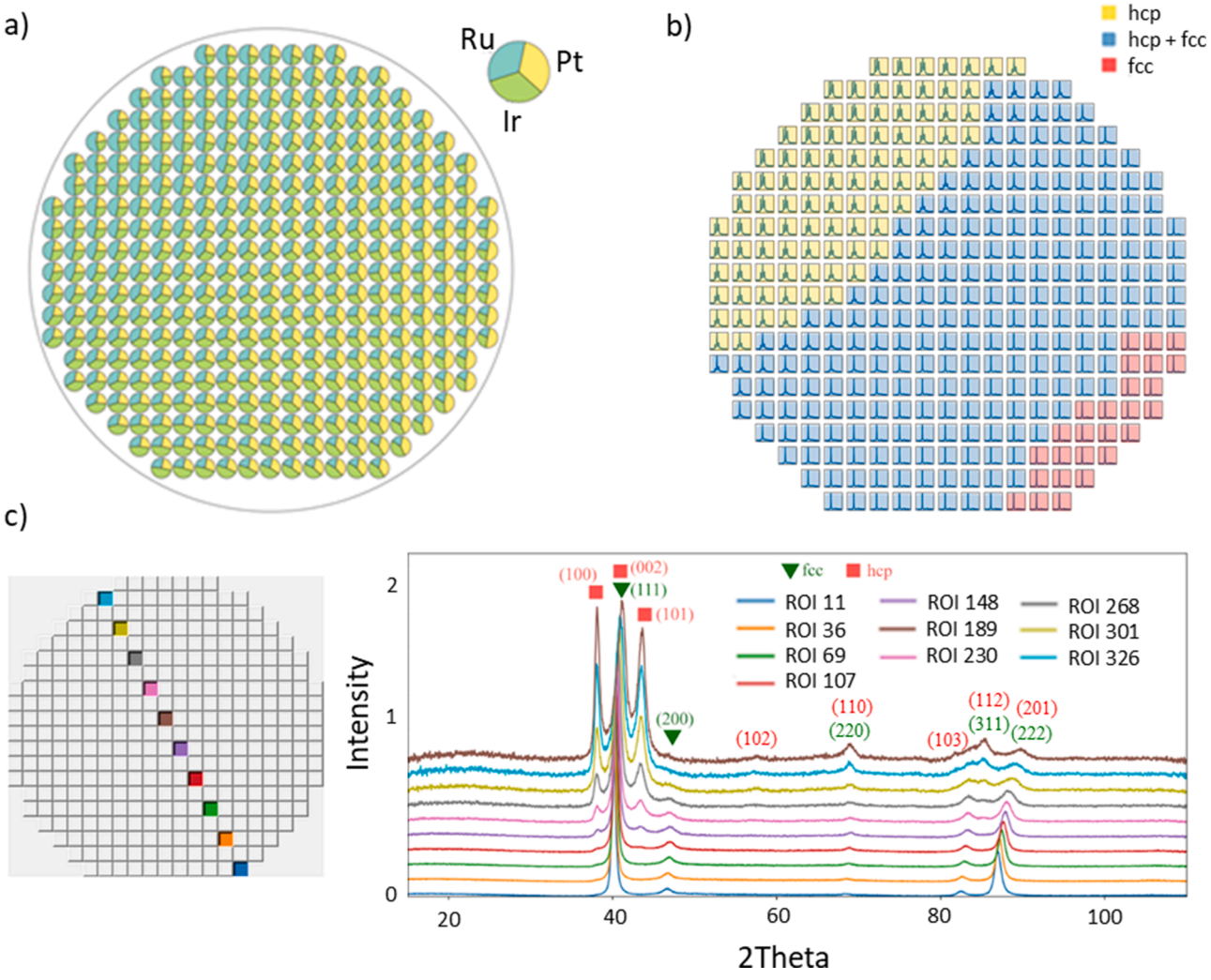

Fig. 1. (a) Visualisation of the composition space covered in the Pt-Ru-Ir material library. The composition spread in between $Pt_{19–50}Ru_{19–59}Ir_{19–48}$. (a) The pie-chart diagram indicates the relative elemental compositions at each of the 342 ROIs. The legend shows the locations of the elemental sputter sources with respect to the substrate. (b) Phase and XRD map show library is crystalline and composed of either pure hcp, pure fcc, or mixed hcp + fcc phase. The legend indicates the respective element positions during deposition. (c) View of XRD patterns along bottom-right to top-left.

3. Results

3.1. Material preparation and physical characterisations

3.1.1. Composition-structure relations in as-deposited Pt-Ru-Ir thin-film material library

A comprehensive Pt-Ru-Ir material library in the compositional region of Pt, Ru and Ir has been synthesised and characterised. As the state-of-art catalyst for isopropanol oxidation is Pt_1Ru_1, the Pt-Ru-Ir library was designed not to deviate far from the centre of interest (equimolar composition). This condition leads to a limitation in the range of metals in the library to approx. 20 – 60 at%. Across the 342 ROIs, the Pt content ranges from 19 to 50%, Ru content from 19 to 59%, and Ir content from 19 to 48% (colour-coded scatter diagrams are shown in Fig. S1). The accuracy (about 1 at.% experimental error) of this quantitative composition analysis is not affected by the substrate because the substrate elements (Si and O) have different X-ray emission peaks than those of the elements the film contains. Based on this, the complete composition range of the material library is written as $Pt_{19–50}Ru_{19–59}Ir_{19–48}$. To better visualise the relative elemental proportions across the library, a pie chart diagram for all 342 ROIs is plotted in Fig. 1a. In each pie chart, the arc length of a slice is proportional to the element content it represents.

The XRD patterns for all 342 ROIs in the as-deposited Pt-Ru-Ir material library are displayed in Fig. 1b. The diffraction peaks in the 2θ range from 38° to 53° are characterised by Bragg reflections from fcc- and hcp-phases. The phase map in this figure is based on comparing experimental diffraction peaks with references from the ICSD database. Clear phase boundaries are observed across the library: (1) pure hcp phase on the right-top side of the library, (2) mixed hcp + fcc phases in the middle, and (3) pure fcc phase on the left-bottom side. A cut along bottom-left to top-right across the phase boundaries is selected and enlarged in Fig. 1c to distinguish more details better. The most intense reflection of (002) was found for hcp at around 40° This peak is located between two other intense reflections of (001) and (101). In the case of the fcc phase, the diffraction patterns exhibit the highest intensity reflection along the (111) plane. Based on the XRD analyses, we conclude that the as-deposited material library is crystalline and comprises phase regions of (I) pure hcp, (II) pure fcc, and (III) a mixed phase region of hcp + fcc.

3.1.2. Carbon-supported nanoparticulate catalysts

The preparation of the trimetallic catalysts is based on two sequential processes. The first process is the deposition of Ru and Ir metal shells on Pt nanoparticle cores, which are supported on carbon microparticles (Pt/C 40 wt%, Hispec). The second process is the diffusion of Ru and Ir shells into the Pt core to obtain intermixed alloy particles by annealing under an H_2 atmosphere. In order to perform the first process, Pt/C was dispersed in isopropanol solvent by mechanically stirring for 1 h at 75 °C. Before dispersion in isopropanol, Pt/C is wetted with just enough water to avoid flammability of isopropanol when contacting with dry Pt/C. In the next step, the precursor aqueous solution of Ru^{3+} and Ir^{3+} ions is added to Pt/C dispersion to form the reaction solution under stirring. To prevent a displacement of Ru by Ir, the salt concentration was kept as high as possible to limit the water concentration in the overall reaction solution. The Ru and Ir deposition reaction is performed by stirring at 75 °C for 2 h. Under these conditions, Ru^{3+} and Ir^{3+} ions are simultaneously reduced by isopropanol, depositing on the surface of Pt catalyst particles as described by Eqs. (1) and (2) since Pt catalyses these 2 reactions.

$$2RuCl_3 + 3CH_3CH(OH)CH_3 \rightarrow 2Ru + 3CH_3COCH_3 + 6HCl \quad (1)$$

$$2IrCl_3 + 3CH_3CH(OH)CH_3 \rightarrow 2Ir + 3CH_3COCH_3 + 6HCl \quad (2)$$

This step produces Ru-Ir deposited on Pt particles supported on C (referred to as RuIr@Pt/C) as observed in STEM-EDXS spectrum images shown in Fig. S2 a, b, c, d, and e. To perform the second process, i.e. the: diffusion of Ru and Ir into Pt particles to form alloy particles, the precatalyst RuIr@Pt/C was annealed at 350 °C under an H_2/Ar atmosphere for 2 h. As observable in Fig. 2 and Fig. S2, f, g, h, i, and j, Ir, Ru, and Pt are well distributed within each catalyst particle. With this method, four $Pt_1Ru_1Ir_x/C$ (x = 0.25, 0.5, 1.0, and 1.5) catalysts were synthesised. The results of the TEM investigation showed that the catalysts are Pt-Ru-Ir alloy nanoparticles loaded on carbon micro-particles. The sizes of Pt-Ru-Ir alloy nanoparticles range from 2 to 10 nm, and they are well distributed over the carbon support, as shown in Figs. S2 and S3. This morphology is analogous to typical Pt/C catalysts for fuel cell applications. The real catalyst composition was measured by SEM-EDXS, shown in Fig. S4. The results align well with the nominal composition.

3.2. Activity mapping of the Pt-Ru-Ir library towards isopropanol electro-oxidation

Activity measurements of ten representative points from this library are depicted in Fig. S5. The spots were chosen to cover the broadest compositional range in the library. The atomic distribution of single elements and the rationale behind the order of measurements (shown by arrows) can be found in the supporting information in Fig. S1. Current densities at the low potential (0.25 V_{RHE}) of the first oxidation peak were compared for each CV of the measured spot from the material library. These values are depicted in a ternary diagram in Fig. 3, together with six selected CVs representing shape variations throughout the library with visually marked points of the current density of the interest. Additionally, results obtained from binary alloys (Pt-Ru, Pt-Ir, Ru-Ir) are shown inside squares for a direct comparison with presented results on the ternary system. Each graph contains measurements of two neighbouring spots. The blank and isopropanol (IPA) correspond to cyclic voltammetry measurements without and with isopropanol, respectively. The obtained currents were normalised by the geometric surface area (SFC parameter). ECSA should not deviate much from the geometric area for the flat surface; therefore, the areas could be interchanged. Laser profilometry measurement shown in Table S2 showed that the surface enlargement due to roughness is only 1.3 – 2.8%, which confirms the negligible contribution. The composition shown in Fig. 3f (and four more shown in Fig. S5) shows no activity towards isopropanol oxidation, as the difference between blank and isopropanol curves is negligible. On the contrary, all compositions (a) – (e) show differences between the two measurements suggesting the activity of the catalyst towards isopropanol oxidation. The highest activity at the low potential (0.25 V_{RHE}) is found for $Pt_1Ru_1Ir_{1.5}$ (Ir-rich) $Pt_{1.5}Ru_1Ir_1$ (Pt-rich) in graphs b) and d), respectively. Overall, $Pt_1Ru_1Ir_{1.5}$ was classified as the most active composition by Pt-Ru-Ir material library screening. To understand the differences in the observed activity of isopropanol oxidation on different compositions, CV shapes can be analysed without the presence of isopropanol depicted in Fig. S6. With increasing Ru and decreasing Ir or Pt content, the H_{upd} area increases, and PtO reduction peak decreases (or is masked by other Faradaic processes) until it entirely disappears. The electrochemically active surface area (ECSA) and capacitive current seem to increase with increasing Ru content in the samples and resemble the CV shape of pure Ru. This shape of the CV seems to correlate also with activity loss. Only compositions with comparable features and thus similarly low surface area (those not resembling CVs of pure Ru) were active.

3.3. Activity measurements of $Pt_1Ru_1Ir_x/C$ nanoparticles and transfer of trends

In order to prove that the compositional trends observed in the thin-film material library can be transferred directly to real-application catalysts consisting of metal nanoparticles dispersed on a porous carbon support, a series of carbon-supported nanoparticles with various Ir contents were synthesised and electrochemically characterised. Since

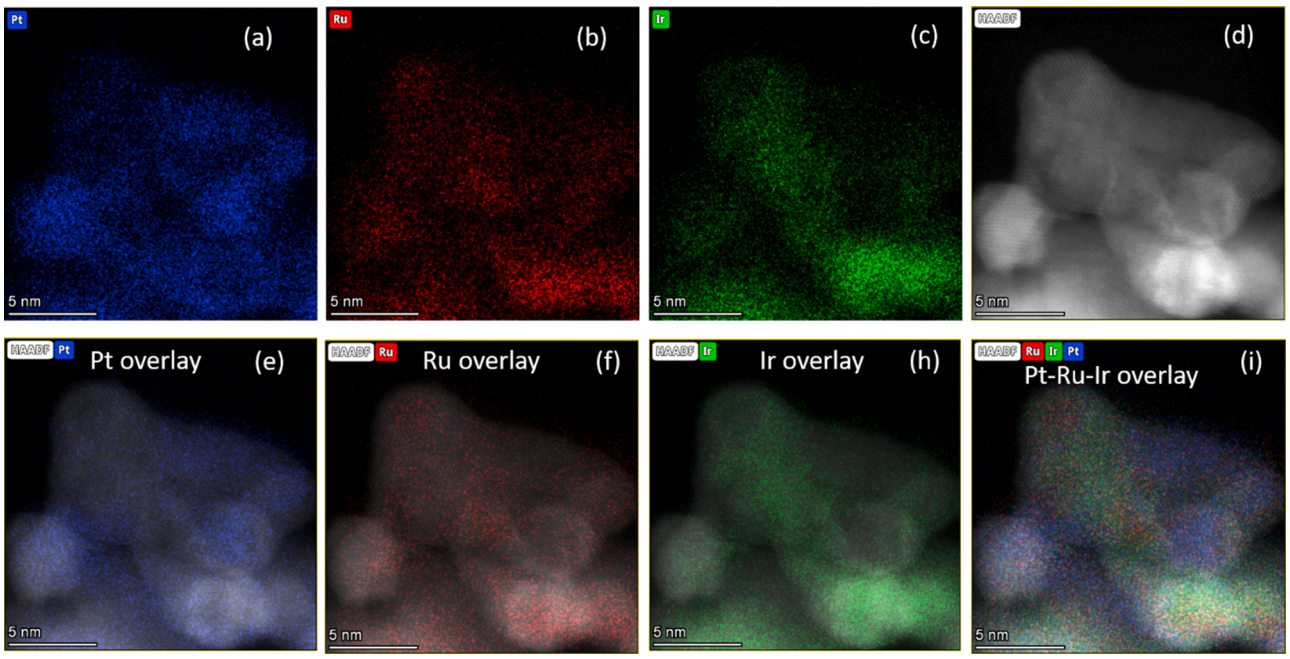

Fig. 2. Compositional analysis of the synthesised carbon-supported $Pt_1Ru_1Ir_{1.5}$ sample. (a), (b), (c), and (d) show Pt, Ir, and Ru elemental maps and HAADF-STEM images of the catalyst particles, respectively, and likewise, (e), (f), (h), and (i) are overlay images of the corresponding elements.

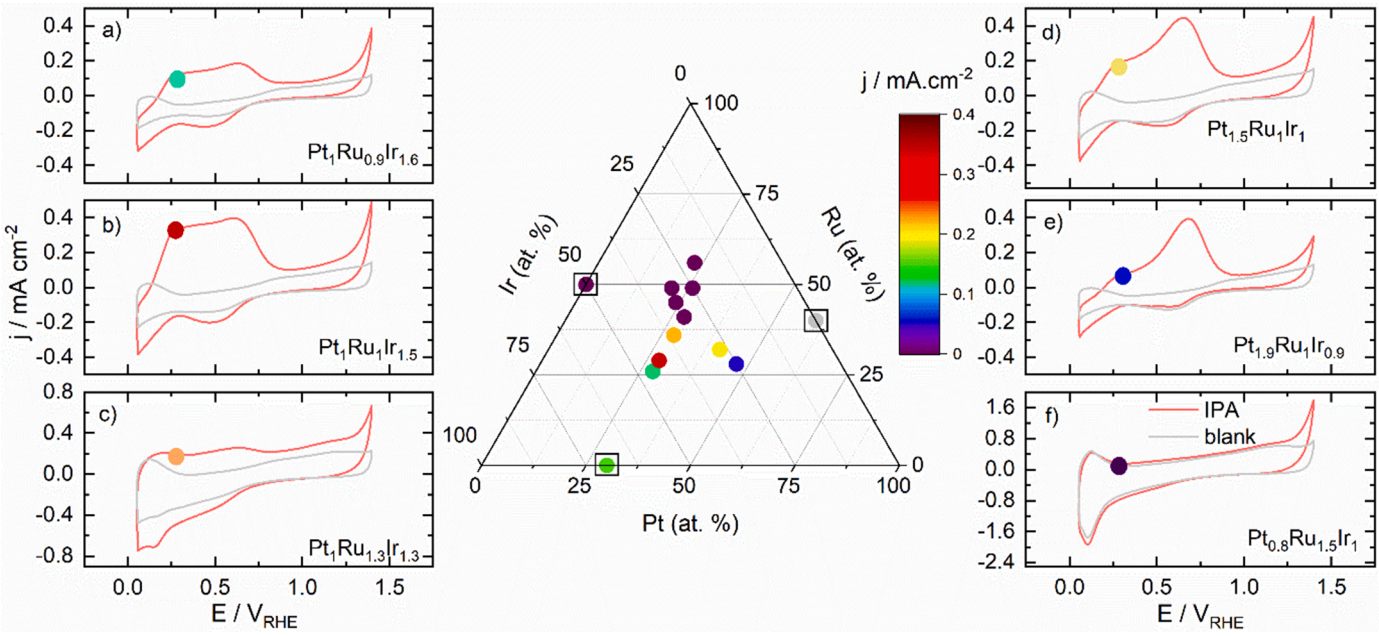

Fig. 3. Cyclic voltammograms recorded for thin-films from the Pt-Ru-Ir library with different compositions in 0.1 M $HClO_4$ both in the absence and presence of 0.1 M isopropanol applying a 50 mV s^{-1} scan rate with a constant Ar purge. Compositions were calculated from the EDX data. Current densities of isopropanol oxidation at 0.25 V_{RHE} vs. compositions are depicted with the colour code in the ternary diagram in the middle (violet representing zero current densities). These points are also marked in each shown CV. Compositions inside the squares represent findings from binary alloys (Ru-Ir shown in this work, Pt-Ir shown in a previous publication [47], and Pt-Ru investigated in our current work depicted by grey as the value is outside of the range, 0.5 mA.cm^{-2}).

the Ir-rich sample was identified as the most active from the thin-film experiments, the focus lies on the synthesis of nanoparticles with different Ir molar ratios with respect to Pt and Ru. Catalysts were studied under the same conditions as thin-films. Firstly, the measurements in the absence of isopropanol are shown in Fig. S7. Overlapping CVs suggest similar ECSA for all four nanoparticulated catalysts. However, the real ECSA can slightly differ due to overlapping features [40]. CO-stripping experiments shown in Fig. S8 (and ECSA values shown in Fig. S9 using Eq. (S1) [40]) show that ESCA decreases with increasing Ir content. This trend can be explained by considering the synthesis procedure – adding each metal to the same Pt/C catalyst. Surface area decreases due to total metal loading being kept the same. Nanoparticles containing more Ir are heavier; therefore, the amount of particles is lower, resulting in lower ECSA for catalysts with more Ir. A comparison of measurements for different compositions in the presence of isopropanol for both systems is shown in Fig. 4. The positive-going scans of the cyclic voltammetry for evaluating the activity of these nanoparticles are shown in Fig. 4a. Current densities were calculated by geometric

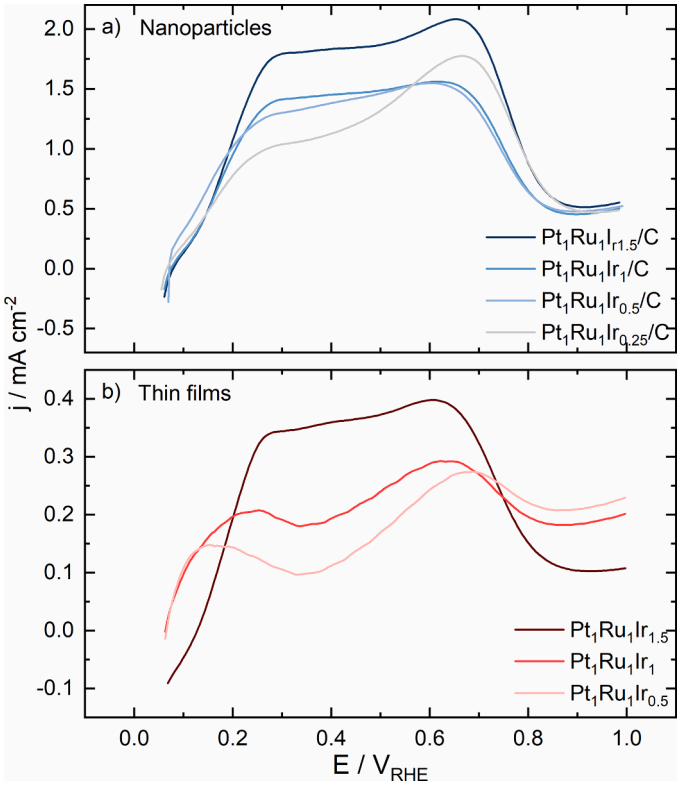

Fig. 4. Positive-going sweeps of the cyclic voltammograms recorded for Pt-Ru-Ir (a) thin-film samples and (b) for nanoparticles with various Ir ratios with respect to Pt and Ru in 0.1 M $HClO_4$ and 0.1 M isopropanol applying a 50 mV s^{-1} scan rate with a constant Ar purge.

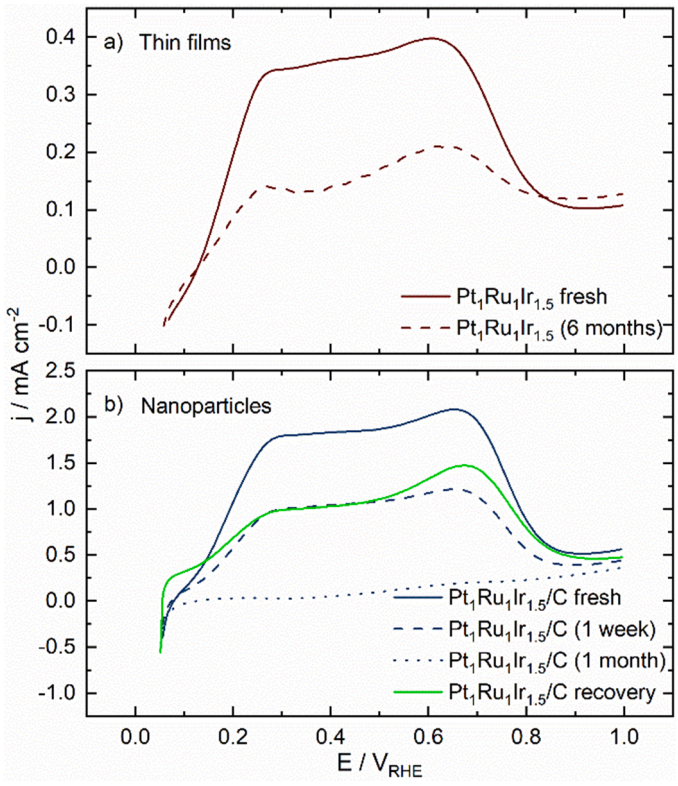

Fig. 5. (a) Positive-going scan of the cyclic voltammogram recorded for a $Pt_1Ru_1Ir_{1.5}$ thin-film composition measured fresh and after six months and (b) cyclic voltammogram recorded on carbon-supported $Pt_1Ru_1Ir_{1.5}$ nanoparticles measured fresh, after one week, after five weeks, and after recovery experiment (– 5 mA cm^{-2}, 5 min) in 0.1 M $HClO_4$ and 0.1 M isopropanol applying a 50 mV s^{-1} scan rate with a constant argon purge.

surface area normalisation. Following the criteria described in Section 3.2, the most active composition is identified as the catalyst with the highest Ir content ($Pt_1Ru_1Ir_{1.5}$/C). Activity decreases with decreasing Ir content. The complete CVs and the comparison of the geometric area and ECSA normalization can be seen in Fig. S10a and b. The trend is the same, but the activity differences are more pronounced in the case of the ECSA normalisation. This underlines that the enhanced activity is caused purely by active metal content and not any other factors.

To confirm the trends further, a series of additional measurements for the thin-film library corresponding precisely to the composition of synthesised nanoparticles (except for $Pt_1Ru_1Ir_{0.25}$/C due to limitations from elemental ranges of the material library) is shown in Fig. 4b. The higher surface area of nanoparticles can explain differences in the current density values compared to thin-films. The trend of increasing activity by increasing Ir content (from $Ir_{0.5}$ to $Ir_{1.5}$) is obvious when comparing Fig. 4a and b. Also, the shape of voltammograms is comparable between the two systems. Therefore, it can be concluded that activity trends from the model system were transferred well into the nanoparticulate catalyst, pointing out the useful combination of thin-film libraries and the SFC for fast screening of compositions for electrocatalytic materials.

3.4. Development of catalyst activity over time

In a prospect of a possible fuel cell application in the future and because longer times are needed between catalyst preparation and measurements, experiments to investigate the possible loss of catalytic activity of the material while left untouched but exposed to the air were conducted for both the sputtered thin-films, and nanoparticle systems. After screening, the materials library was left untouched for six months, and the most active composition was remeasured. Fig. 5a shows that the current density for the measurement performed after six months significantly dropped. A similar experiment was conducted for nanoparticles and is depicted in Fig. 5b. The same drop-casted catalyst was measured right after preparation (fresh), after one week, and after another month. The activity is halved after one week when the catalyst is left untouched and completely lost after one month. A recovery experiment was conducted after 1 month using the same inactive catalytic layer to test whether the activity loss was reversible. A negative current density (– 5 mA cm^{-2}) was applied for 5 min to clean the surface or reduce possible surface oxides. After this, the cyclic voltammogram was recorded again, as also shown in Fig. 5b. The activity loss is partly reversible, and the current densities of the same values as the catalyst being left untouched for a week were recorded. However, the original activity of the fresh catalyst was not reached again. This latter observation should be considered in the future transfer of trends from fundamental investigations into fuel cell tests, where the time difference between catalytic layer preparation and measurement can take multiple days.

To further understand the catalyst deactivation over time described above, the XPS study on the $Pt_1Ru_1Ir_{1.5}$/C catalyst was employed in the same manner. The sample was measured three times: fresh – as drop-casted (AD), after one week, and after one month. The deconvolved high-resolution Pt 4f, Ir 4f, Ru 3d, and C 1s XPS spectra of as drop-casted fresh $Pt_1Ru_1Ir_{1.5}$/C catalyst are shown in Fig. S11, together with assigned binding energies of corresponding peaks. Spectra reveal all elements predominantly in the metallic state with a small contribution of surface oxides, which is inherent for the air-exposed samples.

Fig. S12 compares the XPS spectra acquired for the fresh sample with those for the aged samples. The peak intensity decreases with ageing time for all elements, while the intensity of carbon peak increases, which can be attributed to the adsorption of so-called adventitious carbon on a

metallic surface. On the other hand, there is no significant difference in the shape of recorded spectra except for Pt 4f, which slightly broadens (highlighted by arrows), evidencing increased Pt^{+} contribution. Table S3 summarises the surface relative atomic composition estimated from the integrated areas of the corresponding spectra (considering sensitivity factors) together with values of the ratio between metallic and oxidised states for all elements. The real composition aligns well with the nominal composition (see SI, Fig. S4). The Pt^{0}/Pt^{+} ratio decreased from 6.6 to 2 in one month. In contrast, Ru/Ru^{+} and Ir/Ir^{+} ratios decreased less significantly, suggesting higher oxidation of the Pt surface, which can be attributed to its high reactivity. The composition does not change significantly with ageing. However, slight deviations in favour of mainly Pt (and probably slightly Ir) can be observed after one month. Taking all the above into account, we can state that some segregation of Pt occurs on the surface of the Pt-Ru-Ir catalyst, which can be related to its most pronounced oxidation amongst all elements. However, the conventional XPS instrument cannot fully resolve compositional changes in the outermost layer of the alloy, which is involved in the reaction, because of the relatively high probing depth (around 5 nm).

Even though some oxidation and rearrangements of the metallic surface might be happening, the XPS experiment does not fully explain the observed activity loss over time and the need for a harsh regeneration procedure (applying negative current). In the future, more surface-sensitive techniques will be thus needed to address these deactivation and reactivation processes.

3.5. Screening of stability during dynamic experiments with online ICP-MS

To evaluate stability during dynamic conditions, simulated by CVs, at start/up and shut/down conditions when the dissolution plays the most important role, the upper potential level of the experiment was chosen to be higher than the potential at fuel cell operation. The online ICP-MS stability measurements of the most active, newly synthesised ternary Pt-Ru-Ir/C catalyst were conducted, and the results were compared to the corresponding ones for a commercially available Pt-Ru/C catalyst. The samples were prepared and drop-casted, keeping the same amount of total Pt-Ru content for easier direct comparison. The dissolution in both catalysts during positive and negative-going sweeps up to 1.5 V_{RHE} of two consecutive CVs of Pt, Ru, and Ir in 0.1 M $HClO_4$ is shown in Fig. 6a. The measurement in the presence of 0.05 M isopropanol (lower concentration due to instrument limitations) is shown in Fig. 6b. Both conditions lead to the same dissolution peak shapes; however, the amounts of dissolved Pt and Ru in the presence of isopropanol were doubled. Increased dissolution amounts for Ru in the presence of IPA (for UPL 1.5 V_{RHE}) were also reported in previous work, except for a slightly lower dissolution for the case of Pt [47]. The discrepancies can be explained by the ageing of the commercial catalyst. Upon contact with the catalyst, the dissolution of native oxides (contact peak) is higher, resulting in a slight change of surface composition, which can explain the difference in the trends.

The onset potential of Pt, Ru, and Ir dissolution is 0.91 ± 0.01 V_{RHE}, 0.81 ± 0.04 V_{RHE}, and Ir 0.66 ± 0.07 V_{RHE} (average of two measurements) evaluated from the point at which the first dissolution peak starts to rise. An example of onset potential determination can be found in Fig. S13. As the onset potentials of these two materials overlap, it can be

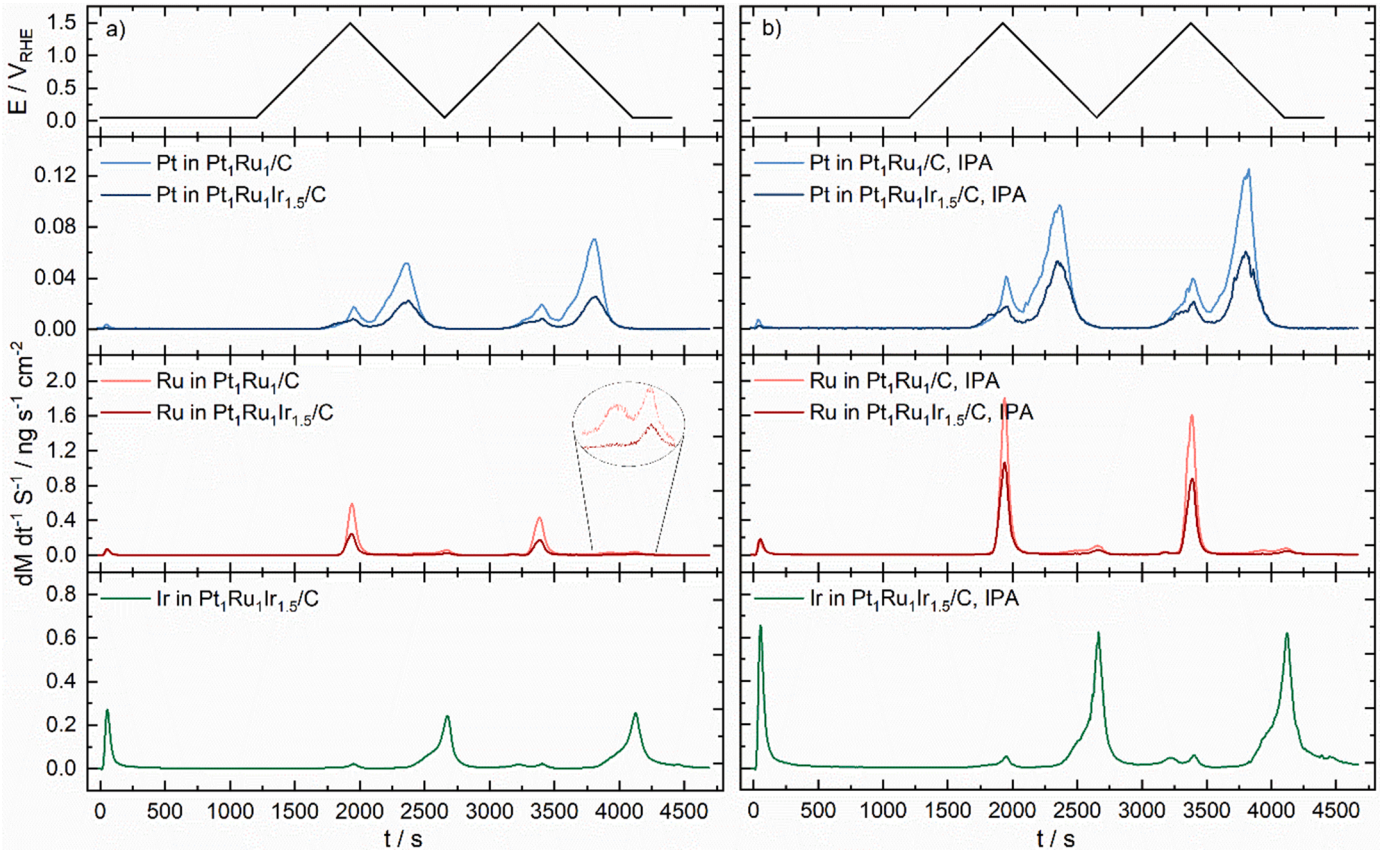

Fig. 6. Online dissolution measurements for Pt, Ru, and Ir in $Pt_1Ru_1Ir_{1.5}/C$ vs. commercial Pt_1Ru_1/C nanoparticles. Dissolution measurements were attained during 2 consecutive CVs (0.05 – 1.5 V_{RHE}, 2 mV s^{-1}) (a) in 0.1 M $HClO_4$, (b) in 0.1 M $HClO_4$ and 0.05 M isopropanol. A magnified section of Ru dissolution in the negative sweep is shown in the circle.

stated that Ir addition does not stabilise the Pt-Ru/C catalyst. Lower dissolution in the Pt-Ru-Ir/C sample could be attributed to the catalyst preparation of nanoparticles and thus lower exposure of Pt and Ru site on the surface compared to commercial Pt-Ru catalyst. Regardless, this will be elaborated on further in the discussion section. Looking at the dissolution features, for Pt, two dissolution peaks can be identified during cycling. First corresponds to Pt dissolution during Pt oxidation until stable PtO_x is formed. The second dissolution peak is attributed to a reduction of PtO_x [48]. Ru and Ir dissolution consists of two separated peaks appearing thanks to the oxidation and reduction of the metal. Potential cycling to more positive potential (1.5 V_{RHE}) results in more distinct featured, doubling of each peak thanks to further oxidation and reduction of metals. All these features are well described and in agreement with previous works on noble metal dissolution [44,47–49]. The only comparative difference between Pt-Ru and Pt-Ru-Ir samples can be seen in a closer look at the Ru dissolution features in a negative sweep, where the Pt-Ru-Ir/C sample is missing one peak corresponding to one of the oxidation processes.

4. Discussion

To identify the role of Ir in Pt-Ru-Ir catalysts, a comparison of cyclic voltammogram shapes of single elements (Pt, Ru, Ir) and binary alloys (Pt-Ru, Pt-Ir, and Ru-Ir) is discussed first. Single metals (SI, Fig. S14) show that Pt is active toward isopropanol oxidation, although the onset of oxidation starts at approximately 0.35 V_{RHE}. On the contrary, Ru and Ir do not show any catalytic activity. However, previous results on isopropanol oxidation using Pt-Ru catalysts showed that the addition of Ru leads to the appearance of an additional oxidation peak of isopropanol at a potential as low as 0.15 V_{RHE} because of the presence of Pt-Ru active sites [20]. The appearance of this oxidation peak at low potential has a different explanation for primary and secondary alcohols. In the case of primary alcohols, like methanol or 1-propanol, the bifunctional mechanism that promotes the oxidation reaction is explained in terms of the necessary adsorption of the reagent on Pt sites. In contrast, Ru sites provide OH species at lower potentials, which aid the oxidation of inhibiting species formed during the dissociative adsorption of the primary alcohol [17,18]. However, this dissociative adsorption does not take place in the case of secondary alcohols, and therefore the promoting effect by Ru in this latter case must have a different explanation. In this case, a different bifunctional mechanism takes place, in which Ru helps to stabilise an O-bound reaction intermediate that lowers the onset potential of the reaction. This stabilisation also takes place in the case of primary alcohols. Still, in this case, the reaction is limited by inhibiting species from dissociative adsorption. In contrast, in the case of a secondary alcohol, oxidation is controlled by the adsorption/dehydrogenation step of the alcohol [21]. However, this oxidation peak at desirably lower overpotentials due to Pt-Ru sites reaching lower current density is due to a fast-poisoning effect by acetone (product) or Ru oxidation, which leads to its appearance in only a narrow potential window [3,20,21].

Similar to Ru, previously published results on the activity of isopropanol using a Pt-Ir thin-film material library showed that for sufficiently high amounts of Ir (15 – 80 at.%), isopropanol is oxidised already at 0.21 V_{RHE}, which can be attributed to Pt-Ir sites. However, current densities do not reach the values of the Pt-Ru catalyst [44]. To complete the picture of isopropanol oxidation on binary catalysts, Ru-Ir was studied, and cyclic voltammograms can be found in Fig. S15. Like Ru and Ir single metals, this catalyst did not show any activity underlining the essential role of Pt in the electrocatalytic oxidation of isopropanol.

Based on the previously described trends that arise from binary catalysts, adding less oxophilic Ir than Ru into Pt-Ru catalyst could enhance oxidation properties of isopropanol oxidation to stabilise further O-bond intermediates, improve acetone desorption, or decrease Ru oxidation at low potential. However, similar to the previously described trends on the Pt-Ru-Ir catalyst for methanol oxidation, the onset potential of isopropanol oxidation was also not shifted to lower values compared to the Pt-Ru catalyst, meaning no expected stabilisation of the O-bound intermediate was observed [21,31]. Nevertheless, the difference in Ir addition can be seen in the area of cyclic voltammograms right after the oxidation peak attributed to Pt-Ru sites [20]. Maximum current density sustained at the same values for a wider potential range compared to Pt-Ru catalyst where current density drops due to Ru oxidation [18,20]. As Ir oxophilicity ranges between Pt and Ru and the onset potential of isopropanol oxidation on Pt-Ir catalyst alone was shifted positively compared to Pt-Ru [44], it is natural to state that the Ir role and contribution in Pt-Ru-Ir is creating another peak arising from Pt-Ir active sites. Ir seems not to stabilise the already-formed intermediate but might create a new reaction pathway with an additional intermediate or possibly decrease the deactivation of Ru sites by its oxidation. Moreover, as suggested by the beneficial effect of Ir on methanol and ethanol oxidation [34,50], Ir could also accelerate the activation of the C—H bond and, thus, hasten one of the rate-limiting steps in the case of isopropanol oxidation. As can be seen from Fig. 3, not all compositions led to the described beneficial effect of Ir addition. Only the composition with 2 Pt, 2 Ru, and 3 Ir neighbouring atoms (assuming equal atoms distribution) benefits the most from the impact of Ir addition and sustains the highest current density attributed to Pt-Ru active sites. The same effect was observed for nanoparticles.

Regarding the stability of the Pt-Ru-Ir catalyst, a study of methanol oxidation showed that Ir could increase the durability of catalysts due to its relatively high oxidation potential [50]. To test this finding, the stability of the Pt-Ru-Ir/C catalyst was compared to commercially available Pt-Ru/C to evaluate the Ir stabilisation effect. As neither the visual onset potential shift for Pt and Ru dissolution nor a significant peak shape difference was observed during the dissolution experiment, further analysis will be discussed to safely exclude the proposed option of the Ir stabilisation effect. Given the remarkably smaller dissolution of Pt-Ru-Ir/C in Fig. 6, a further discussion can elucidate possible reasons for differences in total dissolution amounts. Considering the subsequent addition of Ru and Ir on top of Pt/C and homogenous deposition during $Pt_1Ru_1Ir_{1.5}$/C synthesis (a gradual increase of metal loading on carbon support), the same amount of Pt-Ru in both prepared catalytic layers should also result in the same amount of nanoparticles. This would indicate that the decreased dissolution of Pt and Ru in the Pt-Ru-Ir/C catalyst is caused by smaller exposure of each element on the nanoparticle surface.

To see whether the lower Pt and Ru surface coverage in Pt-Ru-Ir/C is responsible for the observed lower dissolution rates, dissolution profiles were integrated. The obtained amounts were normalised by either the exposed geometric surface area of the working electrode or the molar fraction of the given element in the catalyst determined by XPS. The total dissolution amount recorded during ICP-MS experiments and normalised to the exposed geometric surface area can be seen in Fig. 7a and b, where the differences between catalysts are still noticeable. By normalising these values by surface molar fractions ($Pt_{0.27}Ru_{0.23}Ir_{0.5}$/C or $Pt_{0.5}Ru_{0.5}$/C, assuming identical bulk and surface composition), Fig. 7c and d were obtained. The differences between dissolved amounts of Pt and Ru in the two samples completely vanished. Therefore, it can be concluded that Ir addition has no stabilisation effect on the Pt-Ru catalyst. Expectedly, the higher dissolution in isopropanol presence is still visible, which is in line with previous reports and not a direct focus of this work.

Despite neutral results from dissolution studies, the findings that the addition of Ir does not influence the onset of Ru and Pt dissolution might be correlated to activity results. The addition of Ir also does not shift the onset potential of isopropanol oxidation as shown in this work or previous work stating increased activity for alcohol oxidation but no shift of the onset potential of oxidation [31]. This could serve as a guideline in activity vs. stability relations for further development of future catalysts. However, more comparative studies like this have to be done to confirm the robustness of this hypothesis.

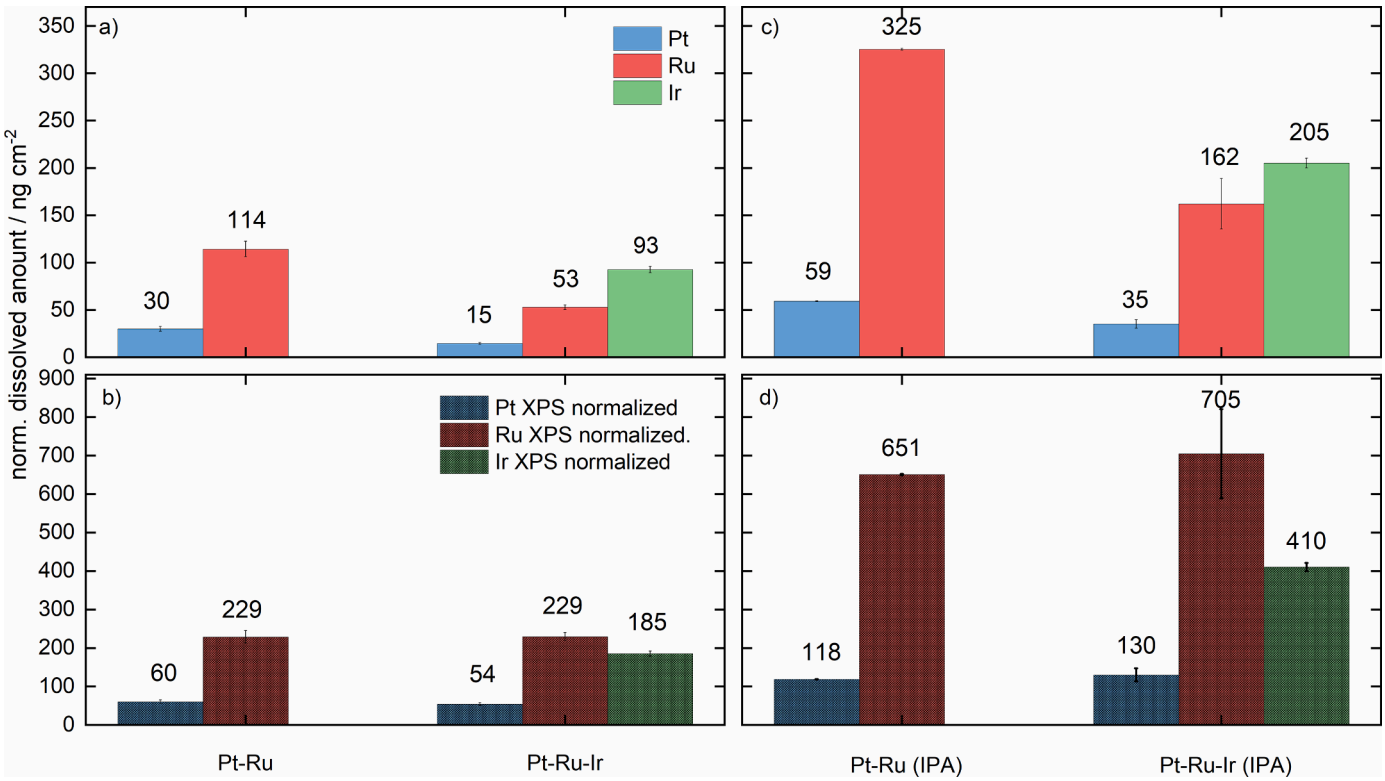

Fig. 7. Dissolved amount calculated from online dissolution measurements of Pt (blue), Ru (red), and Ir (green) in $Pt_1Ru_1Ir_{1.5}$/C vs. commercial Pt_1Ru_1/C nanoparticles by integrating each dissolution feature. Dissolution measurements were attained during two consecutive CVs (0.05 – 1.5 V_{RHE}, 2 mV s^{-1}) a) in 0.1 M $HClO_4$, (b) in 0.1 M $HClO_4$ with surface composition (from XPS) normalised integrated amounts c) in 0.1 M $HClO_4$ and 0.05 M isopropanol, (d) in 0.1 M $HClO_4$ and 0.05 M isopropanol with surface composition (from XPS) normalised integrated amounts.

5. Conclusions

This work explored the Pt-Ru-Ir catalysts of varying composition for a potential future application in the isopropanol fuel cell. The activity of isopropanol oxidation with respect to composition was first studied using the thin-film materials library. During the screening, $Pt_1Ru_1Ir_{1.5}$ was identified as the most active composition at low potential. The addition of Ir resulted in the current density sustaining high in a wider potential range after reaching the oxidation peak attributed to Pt-Ru active sites compared to a state-of-art catalyst for alcohol oxidation, Pt_1Ru_1. A series of $Pt_1Ru_1Ir_x$/C nanoparticles were synthesised to confirm the thin-film model system results. Here, the same composition performed the best in both systems, highlighting the transferability of trends between the model system and real fuel cell catalyst. The benefit of Ir addition on activity and stability during dynamic conditions was discussed extensively. As the oxidation of isopropanol starts at the same onset potential, we can exclude an option of further stabilisation of O-bound intermediates by Ir and instead talk about new active Pt-Ir sites creating an additional peak between the two well-described peaks in the Pt-Ru catalyst. Dissolution results on the best-performing catalyst showed that surface-normalised dissolution was identical to the Pt-Ru commercial catalyst, suggesting no stabilisation effect of Ir addition in terms of catalyst stability. Thanks to the lower exposure of each metal at the surface, their overall dissolution was lower. As the main focus of this work was the activity and stability of Pt-Ru-Ir catalysts, in our future work, product poisoning, another non-negligible part of catalyst improvement, will be explored in the field of alcohol oxidation in the prospect of a fuel cell application.

CRediT authorship contribution statement

Mária Minichová: Conceptualization, Methodology, Validation, Formal analysis, Investigation, Data curation, Writing – original draft, Visualization. **Chuyen Van Pham:** Resources, Investigation, Writing – review & editing. **Bin Xiao:** Resources, Writing – review & editing, Investigation. **Alan Savan:** Resources, Writing – review & editing. **Andreas Hutzler:** Resources, Writing – review & editing, Investigation. **Andreas Körner:** Resources, Writing – review & editing, Investigation. **Ivan Khalakhan:** Resources, Writing – review & editing, Investigation. **Miquel Gamón Rodríguez:** Resources. **Iosif Mangoufis-Giasin:** Writing – review & editing. **Valentín Briega-Martos:** Conceptualization, Methodology, Writing – review & editing, Supervision. **Attila Kormányos:** Conceptualization, Methodology, Writing – review & editing, Supervision. **Ioannis Katsounaros:** Writing – review & editing. **Karl J.J. Mayrhofer:** Writing – review & editing. **Alfred Ludwig:** Writing – review & editing. **Simon Thiele:** Writing – review & editing, Funding acquisition. **Serhiy Cherevko:** Conceptualization, Methodology, Writing – review & editing, Supervision, Project administration, Funding acquisition.

Declaration of Competing Interest

The authors declare that they have no known competing financial interests or personal relationships that could have appeared to influence the work reported in this paper.

Data availability

Data will be made available on request.

Acknowledgments

We acknowledge Markus Bierling for the SEM-EDXS measurements.

This work was funded by the Bavarian Ministry of Economic Affairs, Regional Development and Energy. IK would like to thank the Czech Science Foundation for financial support under project no. 22-03643S

Supplementary materials

Supplementary material associated with this article can be found, in the online version, at doi:10.1016/j.electacta.2023.142032.

References

[1] M.R. Hannah Ritchie, P. Rosado, CO2 and greenhouse gas emissions, OurWorldInData.org, https://ourworldindata.org/co2-and-other-greenhouse-gas-emissions, 2020.
[2] E. Rivard, M. Trudeau, K. Zaghib, Hydrogen storage for mobility: a review, Materials 12 (2019) 1973 (Basel).
[3] G. Sievi, D. Geburtig, T. Skeledzic, A. Bösmann, P. Preuster, O. Brummel, F. Waidhas, M.A. Montero, P. Khanipour, I. Katsounaros, J. Libuda, K.J. J. Mayrhofer, P. Wasserscheid, Towards an efficient liquid organic hydrogen carrier fuel cell concept, Energy Environ. Sci. 12 (2019) 2305–2314.
[4] H. Hoster, T. Iwasita, H. Baumgärtner, W. Vielstich, Pt–Ru model catalysts for anodic methanol oxidation: influence of structure and composition on the reactivity, Phys. Chem. Chem. Phys. 3 (2001) 337–346.
[5] N.V. Long, M. Nogami, Y. Yang, The development of mixture, alloy, and core-shell nano-catalysts with the support nano-materials for energy conversion in low temperature fuel cells, Nano-Compos. (2013).
[6] J. Mueller, H. Hoffmannová, T. Hiratoko, P. Krtil, T. Jacob, Structural evolution of a PtRu catalyst in the oxidation of an organic molecule, J. Catal. 398 (2021).
[7] B.G. Abraham, R. Bhaskaran, R. Chetty, Electrodeposited bimetallic (PtPd, PtRu, PtSn) catalysts on titanium support for methanol oxidation in direct methanol fuel cells, J. Electrochem. Soc. 167 (2020), 024512.
[8] Y.H. Ahmad, A.T. Mohamed, A. Alashraf, M. Matalqeh, A. El-Shafei, S.Y. Al-Qaradawi, A.S. Aljaber, Highly porous PtPd nanoclusters synthesized via selective chemical etching as efficient catalyst for ethanol electro-oxidation, Appl. Surf. Sci. 508 (2020), 145222.
[9] L. Jiang, G. Sun, Z. Zhou, W. Zhou, Q. Xin, Preparation and characterization of PtSn/C anode electrocatalysts for direct ethanol fuel cell, Catal. Today 93 (2004) 665–670.
[10] J.H. Kim, S.M. Choi, S.H. Nam, M.H. Seo, S.H. Choi, W.B. Kim, Influence of Sn content on PtSn/C catalysts for electrooxidation of C1–C3 alcohols: synthesis, characterization, and electrocatalytic activity, Appl. Catal. B 82 (2008) 89–102.
[11] D. González-Quijano, W.J. Pech-Rodríguez, J. González Quijano, J.I. Escalante-Garcia, C. Morais, T.W. Napporn, F.J. Rodríguez-Varela, Performance and *in situ* FTIR evaluation of Pt-Sn/C electrocatalysts with several Pt: Sn atomic ratios for the ethanol oxidation reaction (EOR) in acid media, ChemElectroChem 5 (2018).
[12] Y. Zhu, L. Bu, Q. Shao, X. Huang, Structurally ordered Pt3Sn nanofibers with highlighted antipoisoning property as efficient ethanol oxidation electrocatalysts, ACS Catal. 10 (2020) 3455–3461.
[13] S. Wasmus, A. Küver, Methanol oxidation and direct methanol fuel cells: a selective review1In honour of Professor W. Vielstich on the occasion of his 75th birthday and in appreciation of his contributions to electrochemistry as well as fuel cell development.1, J. Electroanal. Chem. 461 (1999) 14–31.
[14] T.E. Shubina, M.T.M. Koper, Co-adsorption of water and hydroxyl on a Pt2Ru surface, Electrochem. Commun. 8 (2006) 703–706.
[15] P. Waszczuk, G.Q. Lu, A. Wieckowski, C. Lu, C. Rice, R.I. Masel, UHV and electrochemical studies of CO and methanol adsorbed at platinum/ruthenium surfaces, and reference to fuel cell catalysis, Electrochim. Acta 47 (2002) 3637–3652.
[16] M. Watanabe, S. Motoo, Electrocatalysis by ad-atoms: part III. Enhancement of the oxidation of carbon monoxide on platinum by ruthenium ad-atoms, J. Electroanal. Chem. Interfacial Electrochem. 60 (1975) 275–283.
[17] H.A. Gasteiger, N. Markovic, P.N. Ross Jr, E.J. Cairns, Methanol electrooxidation on well-characterized platinum-ruthenium bulk alloys, J. Phys. Chem. 97 (1993) 12020–12029.
[18] H.A. Gasteiger, N. Marković, P.N. Ross Jr, E.J. Cairns, Electro-oxidation of small organic molecules on well-characterized Pt-Ru alloys, Electrochim. Acta 39 (1994) 1825–1832.
[19] J. Mathey, (2023) Performance of liquid fuels in a platinum-ruthenium-catalysed polymer electrolyte fuel cell.
[20] P. Khanipour, F.D. Speck, I. Mangoufis-Giasin, K.J.J. Mayrhofer, S. Cherevko, I. Katsounaros, Electrochemical oxidation of isopropanol on platinum–ruthenium nanoparticles studied with real-time product and dissolution analytics, ACS Appl. Mater. Interfaces 12 (2020) 33670–33678.
[21] I. Mangoufis-Giasin, O. Piqué, P. Khanipour, K.J.J. Mayrhofer, F. Calle-Vallejo, I. Katsounaros, Different promoting roles of ruthenium for the oxidation of primary and secondary alcohols on PtRu electrocatalysts, J. Catal. 400 (2021) 166–172.
[22] P. Hauenstein, I. Mangoufis-Giasin, D. Seeberger, P. Wasserscheid, K.J. J. Mayrhofer, I. Katsounaros, S. Thiele, Impact of catalyst loading, ionomer content, and carbon support on the performance of direct isopropanol fuel cells, J. Power Sources Adv. 10 (2021), 100064.
[23] M. Brodt, K. Müller, J. Kerres, I. Katsounaros, K. Mayrhofer, P. Preuster, P. Wasserscheid, S. Thiele, The 2-propanol fuel cell: a review from the perspective of a hydrogen energy economy, Energy Technol. 9 (2021), 2100164.
[24] E. Antolini, Platinum-based ternary catalysts for low temperature fuel cells: part I. Preparation methods and structural characteristics, Appl. Catal. B 74 (2007) 324–336.
[25] T. Kawaguchi, Y. Rachi, W. Sugimoto, Y. Murakami, Y. Takasu, Performance of ternary PtRuRh/C electrocatalyst with varying Pt:Ru:Rh ratio for methanol electro-oxidation, J. Appl. Electrochem. 36 (2006) 1117–1125.
[26] F. Liu, J.Y. Lee, W.J. Zhou, Segmented Pt/Ru, Pt/Ni, and Pt/RuNi nanorods as model bifunctional catalysts for methanol oxidation, Small 2 (2006) 121–128.
[27] W.C. Choi, J.D. Kim, S.I. Woo, Quaternary Pt-based electrocatalyst for methanol oxidation by combinatorial electrochemistry, Catal. Today 74 (2002) 235–240.
[28] M. Götz, H. Wendt, Binary and ternary anode catalyst formulations including the elements W, Sn and Mo for PEMFCs operated on methanol or reformate gas, Electrochim. Acta 43 (1998) 3637–3644.
[29] P. Strasser, Q. Fan, M. Devenney, W.H. Weinberg, P. Liu, J.K. Nørskov, High throughput experimental and theoretical predictive screening of materials – a comparative study of search strategies for new fuel cell anode catalysts, J. Phys. Chem. B 107 (2003) 11013–11021.
[30] S. Liao, K.A. Holmes, H. Tsaprailis, V.I. Birss, High performance PtRuIr catalysts supported on carbon nanotubes for the anodic oxidation of methanol, J. Am. Chem. Soc. 128 (2006) 3504–3505.
[31] P. Sivakumar, V. Tricoli, Pt-Ru-Ir nanoparticles prepared by vapor deposition as a very efficient anode catalyst for methanol fuel cells, Electrochem. Solid State Lett. 9 (2006) A167.
[32] D. Geng, G. Lu, Dependence of onset potential for methanol electrocatalytic oxidation on steric location of active center in multicomponent electrocatalysts, J. Phys. Chem. C 111 (2007) 11897–11902.
[33] E. Reddington, A. Sapienza, B. Gurau, R. Viswanathan, S. Sarangapani, E. S. Smotkin, T.E. Mallouk, Combinatorial electrochemistry: a highly parallel, optical screening method for discovery of better electrocatalysts, Science 280 (1998) 1735–1737.
[34] B. Gurau, R. Viswanathan, R. Liu, T.J. Lafrenz, K.L. Ley, E.S. Smotkin, E. Reddington, A. Sapienza, B.C. Chan, T.E. Mallouk, S. Sarangapani, Structural and electrochemical characterization of binary, ternary, and quaternary platinum alloy catalysts for methanol electro-oxidation, J. Phys. Chem. B 102 (1998) 9997–10003.
[35] A. Lima, C. Coutanceau, J.-.M. Léger, C. Lamy, Investigation of ternary catalysts for methanol electrooxidation, J. Appl. Electrochem. 31 (2001) 379–386.
[36] D. Geng, D. Matsuki, J. Wang, T. Kawaguchi, W. Sugimoto, Y. Takasu, Activity and durability of ternary PtRuIrB C for methanol electro-oxidation, J. Electrochem. Soc. (2009) 156.
[37] F. Ye, C. Xu, G. Liu, J. Li, X. Wang, X. Du, J.K. Lee, A novel PtRuIr nanoclusters synthesized by selectively electrodepositing Ir on PtRu as highly active bifunctional electrocatalysts for oxygen evolution and reduction, Energy Convers. Manage. 155 (2018) 182–187.
[38] Y. Liang, H. Zhang, H. Zhong, X. Zhu, Z. Tian, D. Xu, B. Yi, Preparation and characterization of carbon-supported PtRuIr catalyst with excellent CO-tolerant performance for proton-exchange membrane fuel cells, J. Catal. 238 (2006) 468–476.
[39] Q. Yi, L. Li, W. Yu, Z. Zhou, X. Liu, G. Xu, Hydrothermal synthesis of titanium-supported PtIrRu/Ti electrode and its electrocatalytic activity, J. Alloy. Compd. 466 (2008) 52–58.
[40] Y. Ma, R. Wang, H. Wang, S. Liao, J. Key, V. Linkov, S. Ji, The effect of PtRuIr nanoparticle crystallinity in electrocatalytic methanol oxidation, Mater. 6 (2013) 1621–1631 (Basel).
[41] A. Mechler, A. Topalov, I. Katsounaros, S. Klemm, K. Mayrhofer, A scanning flow cell system for fully automated screening of electrocatalyst materials, J. Electrochem. Soc. 159 (2012) F670–F675.
[42] J.-.P. Grote, A.R. Zeradjanin, S. Cherevko, A. Savan, B. Breitbach, A. Ludwig, K.J. J. Mayrhofer, Screening of material libraries for electrochemical CO2 reduction catalysts – improving selectivity of Cu by mixing with Co, J. Catal. 343 (2016) 248–256.
[43] A.K. Schuppert, A.A. Topalov, A. Savan, A. Ludwig, K.J.J. Mayrhofer, Composition-dependent oxygen reduction activity and stability of Pt–Cu thin films, ChemElectroChem 1 (2014) 358–361.
[44] A. Kormanyos, A. Savan, A. Ludwig, F. Speck, K. Mayrhofer, S. Cherevko, Electrocatalytic oxidation of 2-propanol on PtxIr100-x bifunctional electrocatalysts – A thin-film materials library study, J. Catal. 396 (2021).
[45] K.J. Jenewein, S. Thienhaus, A. Kormányos, A. Ludwig, S. Cherevko, High-throughput exploration of activity and stability for identifying photoelectrochemical water splitting materials, Chem. Sci. 13 (2022) 13774–13781.
[46] S. Geiger, S. Cherevko, A. Topalov, K. Mayrhofer, Dissolution of platinum in presence of chloride traces, Electrochim. Acta 179 (2015).
[47] A. Kormányos, F.D. Speck, K.J.J. Mayrhofer, S. Cherevko, Influence of fuels and pH on the dissolution stability of bifunctional PtRu/C alloy electrocatalysts, ACS Catal. 10 (2020) 10858–10870.
[48] S. Cherevko, S. Geiger, O. Kasian, A. Mingers, K.J.J. Mayrhofer, Oxygen evolution activity and stability of iridium in acidic media. Part 1. – metallic iridium, J. Electroanal. Chem. 773 (2016) 69–78.
[49] S. Cherevko, A.R. Zeradjanin, A.A. Topalov, N. Kulyk, I. Katsounaros, K. J. Mayrhofer, Dissolution of noble metals during oxygen evolution in acidic media, ChemCatChem 6 (2014) 2219–2223.
[50] B. Liu, Z.-.W. Chia, C.-.H. Cheng, J.-.Y. Lee, Promotional effects of Ir addition in carbon-supported Pt5Rh electrocatalysts for the electrooxidation of ethanol at room temperature, Energy Fuels 25 (2011) 3135–3141.